The Astrophysical Journal, 950:114 (14pp), 2023 June 20 https://doi.org/10.3847/1538-4357/acd11c

The Evolving Effect of Cosmic Web Environment on Galaxy Quenching

Farhanul Hasan[1], Joseph N. Burchett[1], Alyssa Abeyta[1], Douglas Hellinger[2], Nir Mandelker[3], Joel R. Primack[2], S. M. Faber[4], David C. Koo[4], Oskar Elek[5], and Daisuke Nagai[6]
[1] Department of Astronomy, New Mexico State University, Las Cruces, NM 88003, USA; farhasan@nmsu.edu
[2] Department of Physics, University of California, Santa Cruz, CA 95064, USA
[3] Centre for Astrophysics and Planetary Science, Racah Institute of Physics, The Hebrew University, Jerusalem 91904, Israel
[4] University of California Observatories and Department of Astronomy and Astrophysics, University of California, Santa Cruz, 1156 High Street, Santa Cruz, CA 95064, USA
[5] Department of Computational Media, University of California, 1156 High Street, Santa Cruz, CA 95064, USA
[6] Department of Physics, Yale University, New Haven, CT 06520, USA
Received 2023 March 13; revised 2023 April 20; accepted 2023 April 24; published 2023 June 15

Abstract

We investigate how cosmic web structures affect galaxy quenching in the IllustrisTNG (TNG100) cosmological simulations by reconstructing the cosmic web within each snapshot using the DisPerSE framework. We measure the comoving distance from each galaxy with stellar mass $\log(M_*/M_\odot) \geqslant 8$ to the nearest node ($d_{\rm node}$) and the nearest filament spine ($d_{\rm fil}$) to study the dependence of both the median specific star formation rate ($\langle {\rm sSFR} \rangle$) and the median gas fraction ($\langle f_{\rm gas} \rangle$) on these distances. We find that the $\langle {\rm sSFR} \rangle$ of galaxies is only dependent on the cosmic web environment at $z < 2$, with the dependence increasing with time. At $z \leqslant 0.5$, $8 \leqslant \log(M_*/M_\odot) < 9$ galaxies are quenched at $d_{\rm node} \lesssim 1$ Mpc, and have significantly suppressed star formation at $d_{\rm fil} \lesssim 1$ Mpc, trends driven mostly by satellite galaxies. At $z \leqslant 1$, in contrast to the monotonic drop in $\langle {\rm sSFR} \rangle$ of $\log(M_*/M_\odot) < 10$ galaxies with decreasing $d_{\rm node}$ and $d_{\rm fil}$, $\log(M_*/M_\odot) \geqslant 10$ galaxies—both centrals and satellites—experience an upturn in $\langle {\rm sSFR} \rangle$ at $d_{\rm node} \lesssim 0.2$ Mpc. Much of this cosmic web dependence of star formation activity can be explained by an evolution in $\langle f_{\rm gas} \rangle$. Our results suggest that in the past ∼10 Gyr, low-mass satellites are quenched by rapid gas stripping in dense environments near nodes and gradual gas starvation in intermediate-density environments near filaments. At earlier times, cosmic web structures efficiently channeled cold gas into most galaxies. State-of-the-art ongoing spectroscopic surveys such as the Sloan Digital Sky Survey and DESI, as well as those planned with the Subaru Prime Focus Spectrograph, JWST, and Roman, are required to test our predictions against observations.

Unified Astronomy Thesaurus concepts: Galaxy evolution (594); Galaxy quenching (2040); Intergalactic filaments (811); Cosmic web (330); Large-scale structure of the universe (902); Star formation (1569); Galaxy formation (595); Hydrodynamical simulations (767); Magnetohydrodynamical simulations (1966)

1. Introduction

In the standard cosmological model, structure formation in the universe occurs at vastly different scales. Galaxies form stars within tens of kiloparsecs and grow inside dark matter (DM) halos that can be 2 orders of magnitude larger. At even larger scales, galaxies and their DM halos are embedded within an intricate network of strand-like filaments, diffuse sheets, dense nodes, and underdense voids, which is termed the "cosmic web" (e.g., Bond et al. 1996; Springel et al. 2005). While the cosmic web has been studied on both theoretical and observational grounds for decades, it remains one of the major outstanding questions in astrophysics whether and how the large-scale cosmic web environment influences the formation and evolution of galaxies.

A chief question in galaxy evolution is how star formation activity proceeds in galaxies and how it ceases, i.e., how quenching occurs. It has long been known that quenching depends on internal mechanisms characterized by the stellar mass M_* or halo mass $M_{\rm vir}$ (e.g., Brinchmann et al. 2004; Cattaneo et al. 2006; Williams et al. 2009; Peng et al. 2010; Darvish et al. 2016), such that galaxy-scale processes, including supernova (SN) and active galactic nucleus (AGN) feedback, can regulate and curtail star formation activity. A widely adopted theoretical viewpoint posits that galaxies in halos with mass $\log(M_{\rm vir}/M_\odot) \gtrsim 11.5$–12 can form stable virial accretion shocks and therefore a hot, hydrodynamically stable circumgalactic medium (CGM) that suppresses accretion of cold gas to the interstellar medium (ISM) necessary for star formation (e.g., Kereš et al. 2005, 2009; Dekel & Birnboim 2006; Dekel et al. 2009; Stern et al. 2020, 2021). Lower-mass galaxies (typically with $\log(M_*/M_\odot) < 10$), especially at high redshifts ($z \gtrsim 2$), lack this ability to form a stable hot CGM and "self-quench" (e.g., Croton et al. 2006; Gabor & Davé 2012).

External processes as characterized by their environment have also emerged as crucial factors in determining how galaxies quench (e.g., Elbaz et al. 2007; Peng et al. 2012; Eardley et al. 2015; Moutard et al. 2018; Bluck et al. 2020). However, the exact nature of the relationship between quenching and environment, and what physical mechanisms manifest this relationship, is a topic of widespread debate. In the hot, dense halos of galaxy groups and clusters, hydrodynamical interactions between the halo medium and satellite galaxies—most notably ram pressure stripping (e.g., Bahé & McCarthy 2015; Boselli et al. 2022)—or tidal interactions between separate galaxies or between galaxies and the halo (e.g., Boselli & Gavazzi 2006; Marasco et al. 2016) can remove the star-forming ISM of a galaxy. Over longer timescales, gas

accretion onto the ISM can be halted, due to lack of accretion from the intergalactic medium (IGM) to the CGM or from the CGM to the ISM via strangulation or starvation (e.g., Larson et al. 1980; Balogh & Morris 2000; Peng et al. 2015).

The cosmic web itself has also been invoked in models of galaxy quenching. Aragon Calvo et al. (2019) proposed that "cosmic web detachment," wherein galaxies are detached from cold-gas-supplying primordial filaments, can explain much of the observed quenching phenomena across time. Song et al. (2021) suggested that close to the edges of filaments there is a coherent, high angular momentum supply of gas to the outer parts of halos, which prevents an efficient transfer of gas from the outer halo to the galactic centers, ultimately quenching these galaxies (see also Peng & Renzini 2020; Renzini 2020). Pasha et al. (2023) found that cosmological accretion shocks at $z \sim 2$–5 can produce a hot ($T > 10^6$ K) IGM at the edge of sheets, which can quench low-mass centrals at these epochs, as shocks around filaments, groups, and clusters sometimes do at lower redshifts (e.g., Birnboim et al. 2016; Zinger et al. 2018; Li et al. 2023).

Studies of the connection between galaxy quenching and the cosmic web in the past decade have yielded mixed results. While many observational studies have found that passive or quenched galaxies are typically located near nodes and filaments (e.g., Kuutma et al. 2017; Kraljic et al. 2018; Laigle et al. 2018; Winkel et al. 2021), some have shown that proximity to cosmic web filaments can also enhance star formation in galaxies (e.g., Darvish et al. 2014; Vulcani et al. 2019). Cosmological hydrodynamical simulations have also provided an inconclusive picture. In the IllustrisTNG simulations (Nelson et al. 2019a), Malavasi et al. (2022) found that the specific star formation rate ($\mathrm{sSFR} = \mathrm{SFR}/M_*$) of galaxies is generally reduced with proximity to nodes and filaments at $z = 0$. Xu et al. (2020) found in the EAGLE simulations (Schaye et al. 2015) a characteristic stellar mass ($\log(M_*/M_\odot) \sim 10.5$) below which galaxies have lower sSFRs in nodes than in filaments and above which this dependence vanishes. Both Kotecha et al. (2022) and Zheng et al. (2022) reported evidence, instead, of filaments increasing star formation activity or at least delaying quenching. Therefore, consensus is yet to be reached on the impact of the cosmic web environment on galaxy quenching and how this varies with stellar mass and redshift.

In this paper, we employ the IllustrisTNG cosmological simulations to study the impacts of the cosmic web environment, particularly of proximity to filaments and nodes, on star formation and gas content in galaxies across cosmic time. We reconstruct the cosmic web in IllustrisTNG using the topologically motivated DisPerSE framework (Sousbie 2011; Sousbie et al. 2011). This is the first study of the dependence of star formation quenching on the cosmic web in the TNG100-1 run across many different redshift snapshots. Malavasi et al. (2022) performed a similar analysis of the TNG300-1 run at $z = 0$.

This paper is organized as follows. In Section 2, we describe the simulation data used in this work and methods of reconstructing the cosmic web. We present our results in Section 3. We discuss the physical interpretations of our results and propose observational tests in Section 4, and conclude in Section 5. We adopt the Planck 2015 cosmology (Planck Collaboration et al. 2016), with $H_0 = 67.74\ \mathrm{km\,s^{-1}\,Mpc^{-1}}$, $\Omega_{\mathrm{M},0} = 0.3089$, and $\Omega_{\Lambda,0} = 0.6911$. All distances are quoted in comoving units, unless stated otherwise.

2. Data and Methods

2.1. TNG Simulations

We analyze outputs from the IllustrisTNG magnetohydrodynamical cosmological simulations, which use the AREPO moving-mesh hydrodynamics code (Springel 2010) to simulate the evolution of gas, stars, DM, and black holes (BHs) from the early universe ($z = 127$) to the present day ($z = 0$). The public data release of the simulations was presented in Nelson et al. (2019a), while introductory results were presented in Pillepich et al. (2018), Nelson et al. (2018), Springel et al. (2018), Marinacci et al. (2018), and Naiman et al. (2018). In particular, we make use of TNG100-1, the highest-resolution run of the TNG100 simulation, which has a box size of ~110.7 comoving Mpc per side; a minimum baryonic and DM particle mass of $\sim 1.4 \times 10^6\, M_\odot$ and $\sim 7.5 \times 10^6\, M_\odot$, respectively; a Planck 2015 cosmology (Planck Collaboration et al. 2016); and 1820^3 initial DM particles. While TNG300-1 provides greater statistics of galaxies and cosmic structures with ≈20 times the volume of TNG100-1, it has approximately one-eighth of the particle mass resolution. On the other hand, TNG50-1 provides ≈16× greater particle mass resolution than TNG100-1, but has approximately one-tenth of the volume.

We obtain galaxy data for all 100 snapshots of the TNG100-1 simulation (hereafter TNG) from the online data repository[7] (Nelson et al. 2019a). In each snapshot, "Group" catalogs are constructed using the friends-of-friends (FoF) substructure identification algorithm, while the SUBFIND algorithm searches for gravitationally bound objects in each FoF group representing either subhalos or the main (host) halo (Springel et al. 2001; Dolag et al. 2009). We make use of both the group and subhalo catalogs to identify halos and galaxies, respectively.

For each snapshot, we set a minimum stellar mass of $\log(M_*/M_\odot) = 8$, which corresponds to a typical minimum observable stellar mass of galaxies in the (nearby) universe and also ensures that the galaxies are well resolved with at least about 100 stellar particles in them. Similarly, we set a minimum halo mass—corresponding to the mass enclosed in a sphere whose mean density is 200 times the critical density of the universe—of $\log(M_{200,\mathrm{c}}/M_\odot) = 9$ to ensure that each of the galaxies in our catalog resides inside halos that are well resolved with at least 100 DM particles. These criteria yield ~50,000 galaxies at $z = 0$ and ~11,000 galaxies at $z = 5$. From these catalogs, we obtain the galaxy comoving position, the star formation rate (SFR), the stellar mass (M_*), the halo mass ($M_{200,\mathrm{c}}$), the halo virial radius ($R_{200,\mathrm{c}}$, the comoving radius at which $M_{200,\mathrm{c}}$ is calculated), and the mass of all gas gravitationally bound to a subhalo (M_{gas}). Hereafter, we refer to subhalos as galaxies and groups as halos.

2.2. Reconstructing the Cosmic Web with DisPerSE

Next, we apply the Discrete Persistent Structures Extractor (DisPerSE) algorithm (Sousbie 2011; Sousbie et al. 2011) to find cosmic web filaments and nodes in each TNG snapshot where at least 10,000 galaxies match our selection criteria above. DisPerSE identifies the topology of space in any given volume based on an input distribution of discrete tracers, which in our case are the spatial locations of all galaxies matching our selection criteria above. To do this, it computes the density field from the inputs, using the Delaunay Tessellation Field

[7] https://www.tng-project.org/data/

Estimator (DTFE; Schaap & van de Weygaert 2000), wherein the entire volume is divided into tetrahedrons, with the positions of individual galaxies as vertices. During the tessellation, the density field at the position of each vertex of the tessellation is smoothed by averaging it with its two nearest neighbors. This is done in order to minimize contamination by shot noise and the detection of small-scale spurious features (see, e.g., Malavasi et al. 2022). DisPerSE calculates the gradient of the density field and identifies critical points where the gradient is zero. These correspond to voids (minima), saddle points, and nodes (maxima) of the density field. Filaments consist of a series of segments connecting maxima to other critical points.

For each topologically significant pair of critical points, DisPerSE computes the persistence, which is defined as the ratio of the density values at the two critical points. Persistence is a simple measure of how robust topological structures, i.e., the identified critical points and filament segments, are to local variations, in this case, of the density field measured from the input galaxy positions. This sets the effective significance level of the detected filaments and allows us to quantify the effect of shot noise in the input data. For our fiducial run, we choose a persistence threshold of 3σ, which has been known to eliminate most spurious filamentary features in the TNG simulations (e.g., Galárraga-Espinosa et al. 2020). By experimenting with cuts of 4σ and 5σ, we find that these miss fainter structures, but nonetheless do not significantly alter our results.

In addition, we choose to apply a smoothing to the positions of the segments of the filamentary skeleton by averaging the initial positions of the extrema of a segment with those of the extrema of contiguous segments. In essence, the skeleton is smoothed by keeping the critical points fixed and averaging the coordinates of each point along a filament with those of its two neighbors. This is done to reduce sharp and/or unphysical shapes of filament segments caused by shot noise. We apply one level of smoothing and find that increasing the amount of smoothing by one level or removing this smoothing does not have a significant effect on our statistical results.

Furthermore, we experiment with varying the minimum stellar mass cut of our galaxy catalog and cosmic web reconstruction, using cuts of $\log(M_*/M_\odot) \geqslant 9$ and $\log(M_*/M_\odot) \geqslant 10$. These are more realistic minimum masses compared to those of large observational surveys such as Sloan Digital Sky Survey (SDSS; e.g., Strauss et al. 2002) DR17 (see, e.g., Wilde et al. 2023 and our Section 4.3). However, the sharp drop in the number of galaxies in TNG with these higher masses yields increasingly fewer input tracers for DisPerSE, which result in far fewer identified filaments and nodes than in our fiducial $\log(M_*/M_\odot) \geqslant 8$ cut, and particularly in very few short filaments (with length <1 Mpc). These higher-mass cuts could therefore bias our results toward more prominent cosmic web features and longer filaments. In practice, varying the minimum $M_{200,c}$ cut is mostly degenerate with varying the minimum M_* cut.

A 2D visual representation of the DisPerSE-identified filaments and nodes superimposed on the distribution of galaxies in TNG is shown in Figure 1. The three panels show $x-y$ projections in a 37 Mpc thick slice (corresponding to about a third of the total thickness) at $z = 0$ (left), $z = 1$ (middle), and $z = 2$ (right). In each panel, the filament spines and nodes are represented by black curves and gray circles, respectively, while galaxies are represented by scatter points, with sizes proportional to M_* and color coding by sSFR.

From this visualization, we can qualitatively assess the spatial distribution of star formation activity in galaxies with respect to cosmic web nodes and filaments. At any redshift, higher-sSFR galaxies are located throughout the volume, whereas lower-sSFR galaxies are almost always located close to a filament spine or a node. From higher to lower redshift (right to left panel), there is a clear decline in global star formation activity, which reflects the decline in cosmic SFR density after the so-called "cosmic noon" thoroughly chronicled in observations (e.g., Madau & Dickinson 2014). The number of massive quiescent galaxies increases considerably from $z = 2$ to $z = 1$ and even more prominently from $z = 1$ to the present day. A rough qualitative visual check shows that virtually all SFR $= 0$ galaxies at low redshift, regardless of mass, live near nodes and/or filaments (we quantify a galaxy's proximity to these cosmic web structures below).

2.3. Defining Distances

To quantitatively study the relationship between the physical properties of a galaxy and its cosmic web environment, we measure two different distances for each galaxy at each snapshot: $d_{\rm node}$, the comoving Euclidean distance from the center of the galaxy to the center of the nearest identified node, and $d_{\rm fil}$, the comoving transverse distance from the center of the galaxy to the nearest identified filament spine. We choose these cosmic-web-centric distance characterizations as they are similar to those of Welker et al. (2020) and Malavasi et al. (2022), among others. Depending on the physical mechanisms affecting star formation quenching, use of physical distances or other parameters such as local gas density, pressure, or angular momentum is also a viable option for the study of the dependence of galaxy properties on the cosmic web environment. In the following, we investigate how star formation quenching and gas reservoirs of TNG galaxies depend on $d_{\rm node}$ and $d_{\rm fil}$ at different masses and redshifts.

3. Results

3.1. Star Formation and Cosmic Web Environment

We first investigate the relationship between star formation activity in galaxies and their proximity to cosmic web structures. In each snapshot, we divide galaxies into three different stellar mass ranges—$8 \leqslant \log(M_*/M_\odot) < 9$, $9 \leqslant \log(M_*/M_\odot) < 10$, and $\log(M_*/M_\odot) \geqslant 10$—and into seven bins of the distances $d_{\rm node}$ and $d_{\rm fil}$. These bins are chosen such that each has an equal number of galaxies. We measure the median sSFR, $\langle$sSFR$\rangle$, for each bin of $d_{\rm node}$ and $d_{\rm fil}$. Experimenting with different numbers of bins, we find the overall results to be insensitive to the number of bins.

The results of these binned statistics are presented in Figure 2, the top row showing $\langle$sSFR$\rangle$ as a function of $d_{\rm node}$ and the bottom row showing $\langle$sSFR$\rangle$ as a function of $d_{\rm fil}$, and each column representing a different mass range. The $\langle$sSFR$\rangle$ are color coded by redshift; vertical error bars represent $\pm1\sigma$ bootstrapped errors on $\langle$sSFR$\rangle$ in each $d_{\rm node}$ or $d_{\rm fil}$ bin, and horizontal error bars represent the width of the bin. Dotted curves represent simple spline interpolations to the $\langle$sSFR$\rangle$–$d_{\rm node}$ and $\langle$sSFR$\rangle$–$d_{\rm fil}$ relations. For a finer look at some intermediate redshifts, each panel also contains an inset showing a color contour plot for each snapshot between $z = 0.5$ and $z = 3$. For certain bins, we show an upper limit on $\langle$sSFR$\rangle$, corresponding to SFR $= 10^{-2.5}\,M_\odot\,{\rm yr}^{-1}$, which is the minimum resolvable SFR (averaged over 200 Myr)

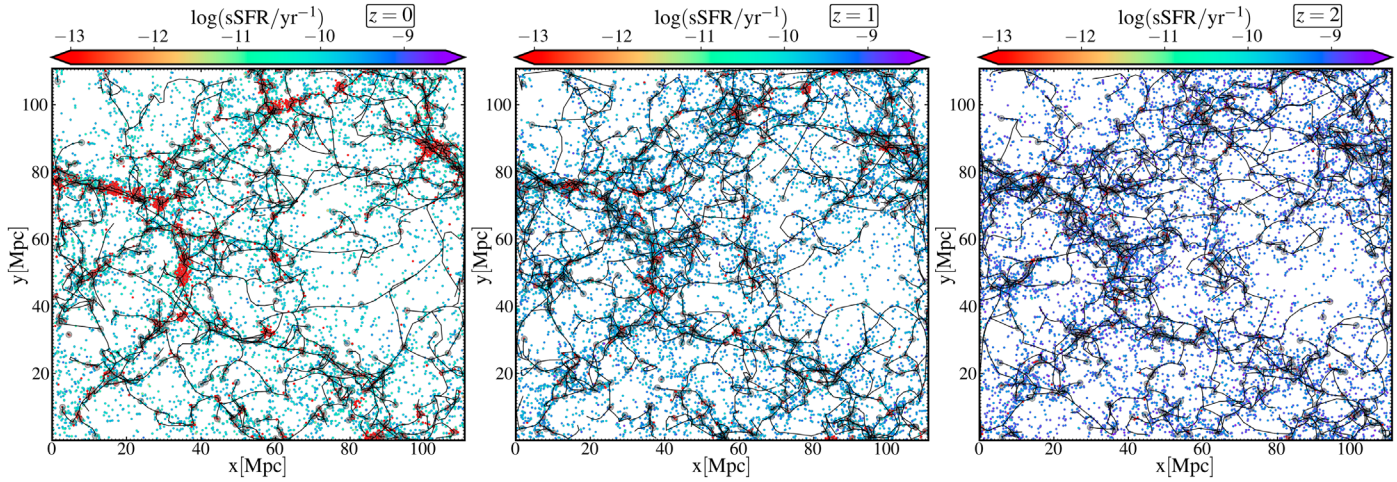

Figure 1. 2D visual representation of galaxies in the TNG100 simulation and cosmic web structures identified by DisPerSE at $z = 0$ (left), $z = 1$ (middle), and $z = 2$ (right). In each panel, filament spines are represented by black curves, and nodes are represented by semitransparent gray circles, while galaxies are represented by scatter points sized by the stellar mass and color coded by sSFR. The same x–y projection of a slice 37 Mpc thick (about a third of the total box width) is shown for each redshift. The global star formation activity declines considerably from higher to lower redshift. Quiescent galaxies at lower redshifts appear to be clustered closer to nodes and filaments.

in TNG due to stochastic star formation with a minimum star particle mass (see Terrazas et al. 2020). For example, for $8 \leqslant \log(M_*/M_\odot) < 9$ galaxies, the maximum upper limit in sSFR is $10^{-11.5}\,\mathrm{yr}^{-1}$, considering the most massive galaxies in this mass range.

In order to separate the effect of nearby nodes from that of filaments alone (because many galaxies that are close to filament spines are also close to nodes), we only consider galaxies that are >1 Mpc away from the nearest node for the bottom row of Figure 2. The choice of 1 Mpc is motivated by two considerations. (1) This is slightly greater than the virial radius $R_{200,c}$ of the most massive galaxy cluster in TNG100. Therefore, this ensures that we remove possible halo-centric effects of nearby clusters and groups (which reside in nodes) and isolates the effect of nearby filaments. (2) This is four times the scale radius of the number density profile of galaxies in filaments derived for TNG300 by Galárraga-Espinosa et al. (2020) and corresponds to a width containing almost all of the matter inside of filaments. We vary this cut to $d_{\rm node} > 0.5$, 1.5, and 2 Mpc as well and find that only galaxies at $z \lesssim 1$ with $d_{\rm fil} < 1$ Mpc show noticeable changes to our quantitative results, while the qualitative results described below remain unchanged. In essence, this $d_{\rm node}$ cut ensures that galaxies at only intermediate to high densities, rather than at extremely high local densities, are considered for the $d_{\rm fil}$ analysis (see Burchett et al. 2020 for an example of how cosmic matter densities relate to different filamentary environments).

First, examining the node-centric relationships, we find that $d_{\rm node}$ is strongly correlated with quenching of star formation in galaxies of all masses at low redshifts ($z \lesssim 0.5$). For $8 \leqslant \log(M_*/M_\odot) < 9$ galaxies at $z \leqslant 0.5$, $\langle$sSFR$\rangle$ vanishes at $d_{\rm node} \lesssim 1$ Mpc. The increase from small to large $d_{\rm node}$ is much more gradual at $z = 1$ ($\approx$3× from $\langle d_{\rm node}\rangle \sim 0.2$ Mpc to $\langle d_{\rm node}\rangle \sim 15$ Mpc). At $z \geqslant 2$, however, there is virtually no dependence of $\langle$sSFR$\rangle$ on $d_{\rm node}$. We note that our results at $z = 0$ are broadly in agreement with those of Geha et al. (2012), who found that in SDSS DR8, almost all quenched galaxies with $7 \leqslant \log(M_*/M_\odot) \leqslant 9$ are found within ∼1.5 Mpc of a massive host.

For intermediate-mass $9 \leqslant \log(M_*/M_\odot) < 10$ galaxies, the trends are similar in that there is a large ∼1 dex rise in $\langle$sSFR$\rangle$ from the smallest to the largest $d_{\rm node}$ bin at $z = 0$, a much smaller rise at $z = 0.5$, and effectively no $d_{\rm node}$ dependence at $z \geqslant 1$. The lack of $d_{\rm node}$ dependence of $\langle$sSFR$\rangle$ at $z > 1$ is also seen for high-mass $\log(M_*/M_\odot) \geqslant 10$ galaxies, but interestingly, these galaxies do not show a monotonic increase in $\langle$sSFR$\rangle$ with $d_{\rm node}$ at lower redshifts. In fact, following a decline with decreasing $d_{\rm node}$ at $d_{\rm node} \gtrsim 0.2$ Mpc, there is an *upturn* in $\langle$sSFR$\rangle$ at $d_{\rm node} \lesssim 0.2$ Mpc.

Considering the filament-centric relationships, we find both differences and similarities with the node-centric relationships. For low-mass galaxies at $z = 0$, there is a sizeable ∼5× increase in $\langle$sSFR$\rangle$ from $\langle d_{\rm fil}\rangle \sim 0.3$ Mpc to $\langle d_{\rm fil}\rangle \sim 15$ Mpc; however, the rise in $\langle$sSFR$\rangle$ with $d_{\rm fil}$ is much smaller at $z = 0$ ($\lesssim$2×) and negligible at $z \geqslant 1$. For the intermediate-mass range, there is effectively no gradient of $\langle$sSFR$\rangle$ with $d_{\rm fil}$ at any redshift. For high-mass galaxies at $z = 0$, we do not see an upturn in $\langle$sSFR$\rangle$ at the smallest $d_{\rm fil}$ (unlike that at small $d_{\rm node}$) but rather a somewhat smooth rise by a factor of a few in $\langle$sSFR$\rangle$ with $d_{\rm fil}$ from small to large $d_{\rm fil}$. At $z > 0.5$, the relationship between $\langle$sSFR$\rangle$ and $d_{\rm fil}$ is very weak. Thus, only low-mass and high-mass galaxies at low redshifts are preferentially quenched near filaments, whereas galaxies of all masses are impacted near nodes.

One of the most striking findings on the star formation–cosmic web connection, seen in both the filament- and node-centric analyses, is the disappearance of a dependence of star formation on distance to cosmic web structures at higher redshifts. The color contour insets included in Figure 2 show the $\langle$sSFR$\rangle$–$d_{\rm node}$ and $\langle$sSFR$\rangle$–$d_{\rm fil}$ relationships for many snapshots at $0.5 \leqslant z \leqslant 3$. These contours flatten out past a certain redshift for all three mass ranges, indicating that star formation activity is essentially independent of proximity to the cosmic web prior to this epoch. The independence of star formation on cosmic web node-centric distance occurs at $z \sim 1.3$ for $9 \leqslant \log(M_*/M_\odot) < 10$ galaxies and at $z \sim 2$ for $8 \leqslant \log(M_*/M_\odot) < 9$ and $\log(M_*/M_\odot) \geqslant 10$ galaxies. The $d_{\rm fil}$ independence of star formation occurs at $z \sim 1$ for low-mass and high-mass galaxies, while the star formation in moderate-mass galaxies does not show any significant $d_{\rm fil}$

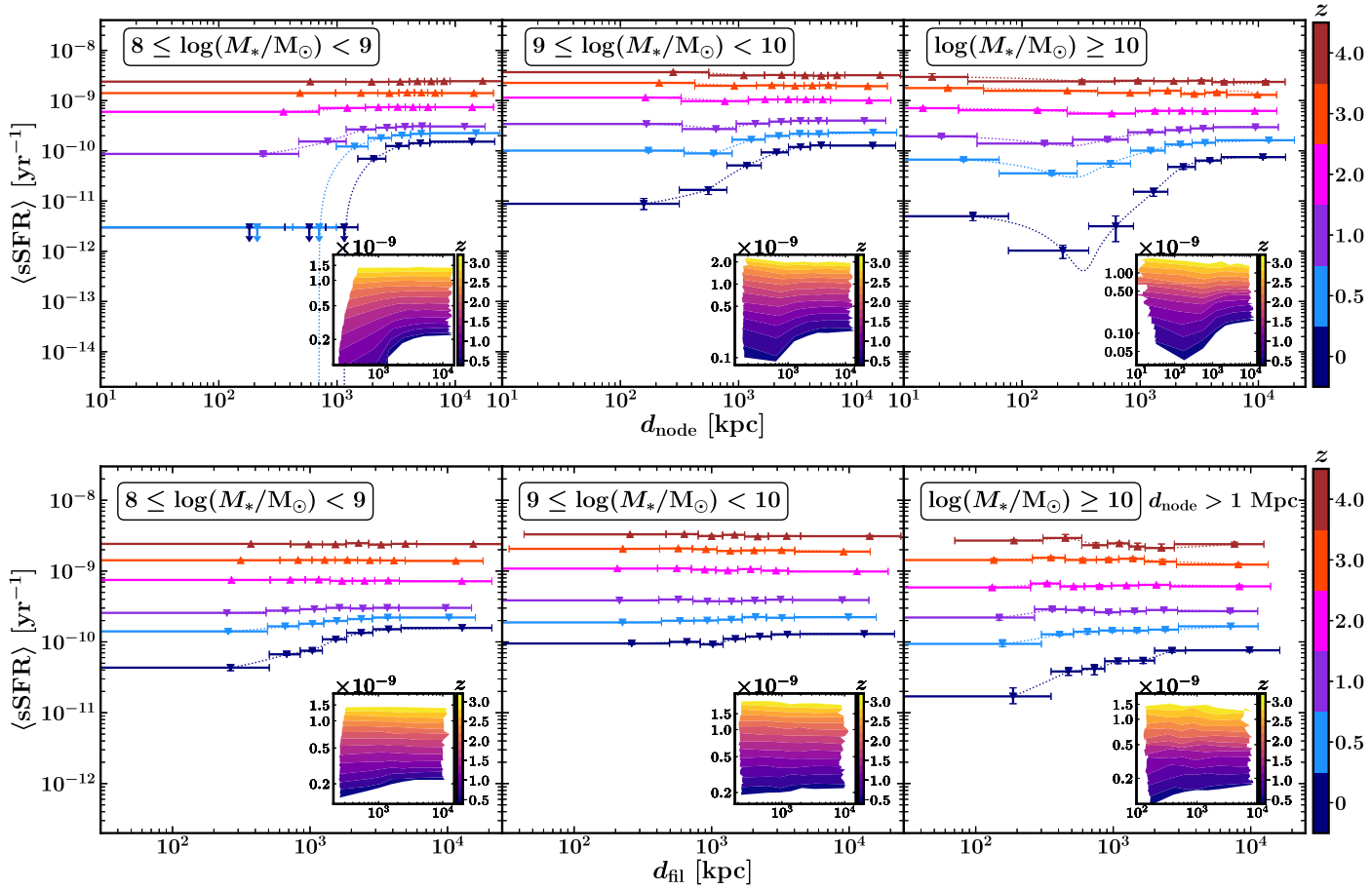

Figure 2. The median sSFR as a function of distance to the nearest node (top row) and filament spine (bottom row) for galaxies with $8 \leqslant \log(M_*/M_\odot) < 9$ (left panels), $9 \leqslant \log(M_*/M_\odot) < 10$ (middle panels), and $\log(M_*/M_\odot) \geqslant 10$ (right panels). The data points and curves are color coded by redshift as indicated by the discrete color bars on the right. Each panel contains an inset that is a continuous color contour plot showing the $\langle \mathrm{sSFR} \rangle$–$d_{\mathrm{node}}$ or $\langle \mathrm{sSFR} \rangle$–$d_{\mathrm{fil}}$ relationship for a larger number of intermediate redshifts, to help locate the redshift at which a distance dependence disappears (see text). Only galaxies with $d_{\mathrm{node}} > 1$ Mpc are included for the filament-centric relationships to mitigate the potential halo-centric effects of nearby clusters and groups. Note that some points are shown as upper limits on $\langle \mathrm{sSFR} \rangle$. Star formation activity is dependent on d_{node} and (to a lesser extent) on d_{fil} only at lower redshifts, while this dependence disappears at $z \geqslant 2$.

dependence at any redshift. From our analysis, it can be deduced that the cosmic web environment began affecting star formation activity during the later stages of, or immediately after, the so-called "cosmic noon" of star formation, when the SFR density in the universe peaked (ending at $z \sim 1.5$; e.g., Madau & Dickinson 2014).

3.2. Central and Satellite Galaxies

We separate our galaxy samples into central and satellite galaxies to investigate how star formation depends on the cosmic web environment for both galaxy types. At each redshift, we identify the most massive galaxy in a halo as the central galaxy and the rest as satellite galaxies and then repeat the analysis in Section 3.1. The $\langle \mathrm{sSFR} \rangle$–$d_{\mathrm{node}}$ and $\langle \mathrm{sSFR} \rangle$–$d_{\mathrm{fil}}$ relationships are shown for central and satellite galaxies in Figure 3. We only include color contour inset plots in the panels where any significant relationship between the cosmic web environment and star formation is seen.

In general, we find that at low redshifts, star formation in satellite galaxies is much more strongly connected to the cosmic web environment than that in central galaxies. At $z < 1$, there is a very modest rise in $\langle \mathrm{sSFR} \rangle$ of low-mass centrals with d_{node} and in intermediate-mass centrals, there is no dependence of $\langle \mathrm{sSFR} \rangle$ on d_{node}. In contrast, star formation is effectively quenched close to nodes in low-mass satellites at $z \leqslant 0.5$, and in intermediate-mass satellites at $z = 0$.

High-mass centrals show a strong correlation between $\langle \mathrm{sSFR} \rangle$ and d_{node} at low redshifts. While the rise in $\langle \mathrm{sSFR} \rangle$ with d_{node} is mostly monotonic at $z = 0$, we see an upturn in $\langle \mathrm{sSFR} \rangle$ at small d_{node} ($d_{\mathrm{node}} \lesssim 0.1$ Mpc) at $z \sim 0.5$–1, similar to that found for the full galaxy population at the lowest redshifts (Figure 2). This upturn is also seen in high-mass satellites at $z = 0$, suggesting that the elevation of star formation activity of high-mass galaxies very close to nodes is applicable for both centrals and satellites (with the caveat that the errors for the satellite relationships are larger). Beyond $d_{\mathrm{node}} \sim 0.1$ Mpc, there is a smooth rise in $\langle \mathrm{sSFR} \rangle$ with d_{node} for satellites at $z \leqslant 0.5$ and for centrals at $z \leqslant 1$.

With respect to filaments, there is negligible dependence of $\langle \mathrm{sSFR} \rangle$ on d_{fil} in centrals of any mass across cosmic time. Both low-mass and high-mass satellites are effectively quenched at small d_{fil} at $z = 0$, while the rise in $\langle \mathrm{sSFR} \rangle$ with d_{fil} is more modest in intermediate-mass satellites. However the small number statistics of the high-mass satellite population prevents us from drawing strong conclusions about their star formation dependence. While satellites appear to drive much of the dependence of star formation on proximity to cosmic web filaments and nodes at low redshifts, there is no statistically

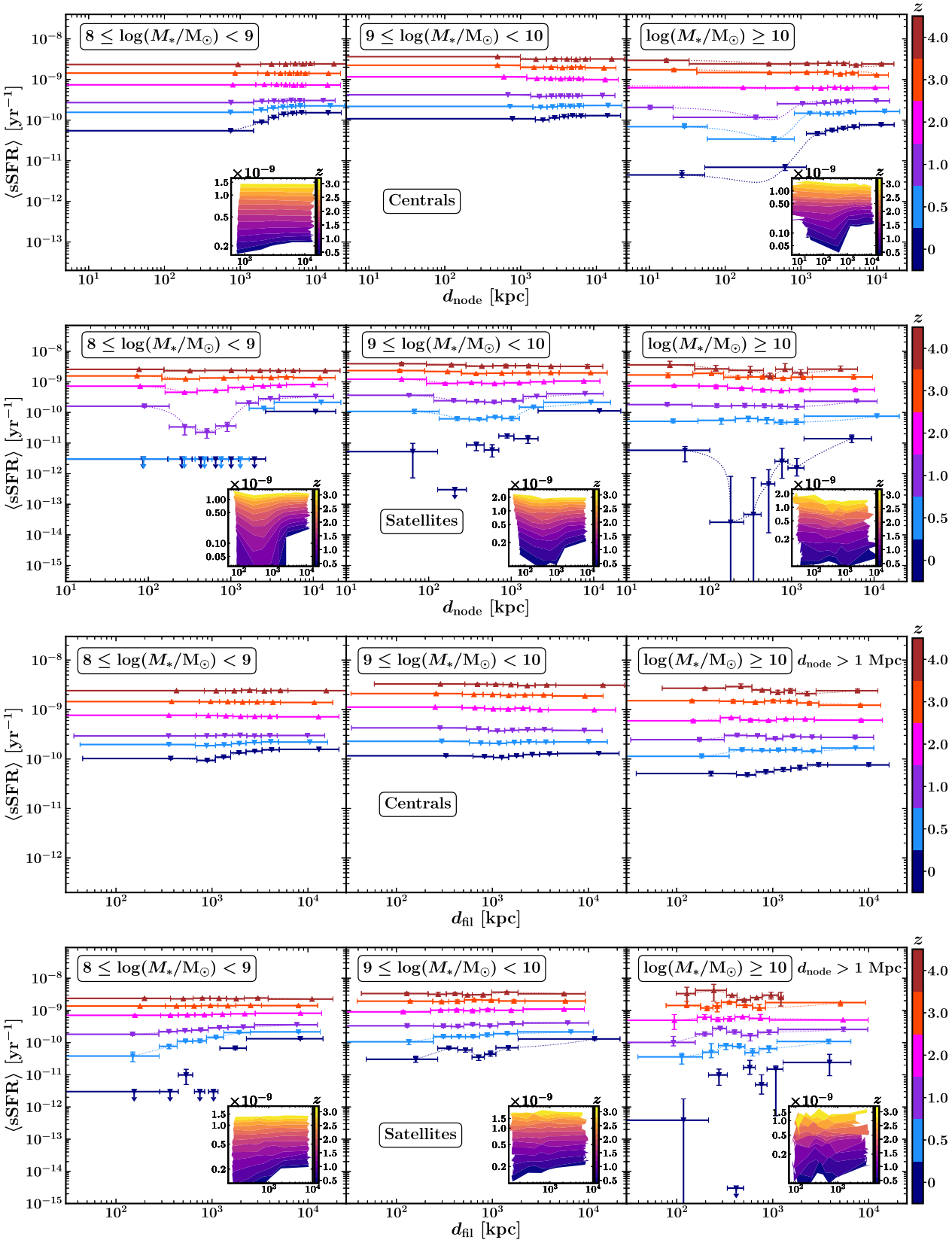

Figure 3. $\langle$sSFR$\rangle$ in bins of d_{node} (top two rows) and d_{fil} (bottom two rows) for central galaxies (first and third rows) and satellite galaxies (second and fourth rows) at different redshifts. Star formation in central galaxies is less dependent on the cosmic web environment than that in satellite galaxies, which are significantly quenched at small d_{node} and d_{fil} at low redshifts. Neither centrals nor satellites exhibit a cosmic web dependence of star formation activity at $z \geqslant 2$. Insets are not included where no significant relationships between the cosmic web environment and sSFR are seen.

significant dependence of star formation on the cosmic web environment at $z \geqslant 2$ for either centrals or satellites.

3.3. Gas Fraction and Cosmic Web Environment

To further investigate the star formation–cosmic web connection, we examine the available gas content in galaxies relative to nodes and filaments. To this end, we measure the gas fraction,

$$f_{\rm gas} = \frac{M_{\rm gas}}{M_{\rm gas} + M_*}, \quad (1)$$

which is the ratio of gas mass to the sum of gas and stellar mass bound to a galaxy. We calculate the median gas fraction, $\langle f_{\rm gas} \rangle$, for all galaxies, centrals, and satellites in the same bins of $d_{\rm node}$ and $d_{\rm fil}$ for the same mass ranges and redshifts above. The $\langle f_{\rm gas} \rangle$–$d_{\rm node}$ and $\langle f_{\rm gas} \rangle$–$d_{\rm fil}$ relationships are presented in Figures 4 and 5, respectively. For clarity of presentation, we only include four redshift bins, $z = 0$, 1, 2, and 4, in these plots. As in Figure 2, the $\pm 1\sigma$ bootstrapped error bars on the medians are shown.

Figure 4 shows that for the full galaxy population, there is a strong dependence of $\langle f_{\rm gas} \rangle$ on $d_{\rm node}$ at lower redshifts. At $z = 0$, low-mass galaxies at $d_{\rm node} \lesssim 1$ Mpc are completely devoid of gas, which explains why they are quenched in these environments. This is mostly driven by satellite galaxies, as low-mass centrals only see a drop of a few percent in $\langle f_{\rm gas} \rangle$ from larger to smaller $d_{\rm node}$. In intermediate-mass galaxies, $\langle f_{\rm gas} \rangle$ drops by an order of magnitude from the largest to the smallest $d_{\rm node}$ bin at $z = 0$, which is commensurate with the $\sim$1 dex drop in $\langle$sSFR$\rangle$ in Figure 2. This is again primarily driven by a dramatic decline in gas fraction of satellites while centrals only exhibit a modest decline.

In high-mass galaxies, we find a minimum in $\langle f_{\rm gas} \rangle$ at $d_{\rm node} \approx 0.7$ Mpc followed by a steep rise at smaller $d_{\rm node}$. This dramatic upturn in gas fraction helps explain the upturn in star formation at small $d_{\rm node}$ at low redshifts, but this turnover (a) is much more pronounced in $\langle f_{\rm gas} \rangle$ than in $\langle$sSFR$\rangle$ and (b) persists out to $z = 4$ for $\langle f_{\rm gas} \rangle$ while it only exists out to $z \sim 1$ for $\langle$sSFR$\rangle$. The relationship between $\langle f_{\rm gas} \rangle$ and $d_{\rm node}$ in high-mass galaxies is largely dictated by central galaxies, which have large gas fractions close to nodes across cosmic time. This, however, does not result in highly enhanced star formation in low-redshift centrals at small $d_{\rm node}$, possibly implying a lack of star formation efficiency in these environments—possibly due to the central AGNs heating the gas in these galaxies and suppressing star formation (see discussion below). High-mass satellites also exhibit a small upturn in $\langle f_{\rm gas} \rangle$ at $d_{\rm node} \lesssim 0.1$ Mpc at $z \leqslant 3$. Unlike star formation activity, the gas fraction in all $\log(M_*/M_\odot) \geqslant 10$ galaxies depends on the proximity to nodes even at $z = 4$.

Proximity to filaments is less strongly correlated with $\langle f_{\rm gas} \rangle$ than proximity to nodes, as shown in Figure 5. At low redshifts, a monotonic rise in $\langle f_{\rm gas} \rangle$ with $d_{\rm fil}$ in low- and intermediate-mass galaxies is caused mostly by the steep rise in satellite population, but this dependence disappears with increasing redshift. Centrals of all masses show virtually no $d_{\rm fil}$ dependence on $\langle f_{\rm gas} \rangle$ at any redshift, consistent with a lack of dependence of star formation activity on distance to filaments.

We also note that the declining availability of gas in galaxies should not immediately result in reduced star formation activity; instead, there should be a time lag between the reduction in gas and the reduction in star formation. This is generally consistent with our results: $\langle f_{\rm gas} \rangle$ decreases at small $d_{\rm node}$ and $d_{\rm fil}$ at higher redshift compared to $\langle$sSFR$\rangle$ for any given stellar mass range. In satellites and even high-mass centrals, a correlation between $\langle f_{\rm gas} \rangle$ and $d_{\rm node}$ exists out to $z = 4$ while star formation is independent of $d_{\rm node}$ at $z \geqslant 2$. Alternatively, these results can be explained by star formation being less efficient further from nodes than closer to nodes at earlier times.

Our results in this section suggest the following: (1) star formation quenching near cosmic web structures is typically preceded by a scarcity of gas, (2) the gas fraction in satellite galaxies is more significantly affected by the cosmic web environment than that in central galaxies and this effect drives the general cosmic web dependence of the gas fraction, and (3) at later times, high-mass galaxies, including both satellites and centrals, are more gas-rich near centers of nodes than at the outskirts, leading to increased star formation closer to nodes.

4. Discussion

4.1. Physical Interpretations

Here, we interpret our results in terms of physical mechanisms governing the evolution of galaxies and the large-scale structure. Perhaps the most puzzling result is that the star formation activity of galaxies in TNG does not depend on their large-scale cosmic web environment at $z \geqslant 2$, in contrast with later times, when significant dependence occurs. At face value, this seems to suggest a rising importance of quenching driven by environment with cosmic time, and indeed, several recent works have found varying degrees of evidence for a lack of small- or large-scale environmental dependence of star formation at higher redshifts—in both observations (e.g., Moutard et al. 2018; Chang et al. 2022; Momose et al. 2022) and simulations (e.g., Xu et al. 2020).

4.1.1. The Cosmic Web Dependence after Cosmic Noon

The low-redshift dependence of star formation activity on $d_{\rm node}$ and $d_{\rm fil}$ can generally be explained by the variation of gas fraction with these distances. In lower-mass galaxies at low redshifts, the monotonic descent in $\langle$sSFR$\rangle$ toward nodes and filaments is consistent with the corresponding descent in $\langle f_{\rm gas} \rangle$. On average, low-mass galaxies that are within several hundred kiloparsecs of a node or filament effectively stop forming new stars at $z = 0$, most likely because they have very little to no gas available to do so, a behavior largely driven by satellites.

This points to a picture where dwarf galaxies that accrete onto the halos of more massive centrals are quenched in overdense environments, where their gas supply is depleted. Dwarf satellites located in galaxy clusters and groups are subjected to harsh gaseous environments dominated by warm and hot gas with high densities and long cooling times. In these environments, a combination of physical processes can act together on the gas reservoirs of dwarf satellites.

Gas may be removed by ram pressure stripping when these galaxies move through the group/cluster medium or by gravitational (tidal) interactions between the satellite and the central galaxy/other satellites or the halo itself. These processes, while often identified as the likely culprits for gas stripping and quenching of low-mass satellites in clusters/groups, typically act on relatively short timescales of

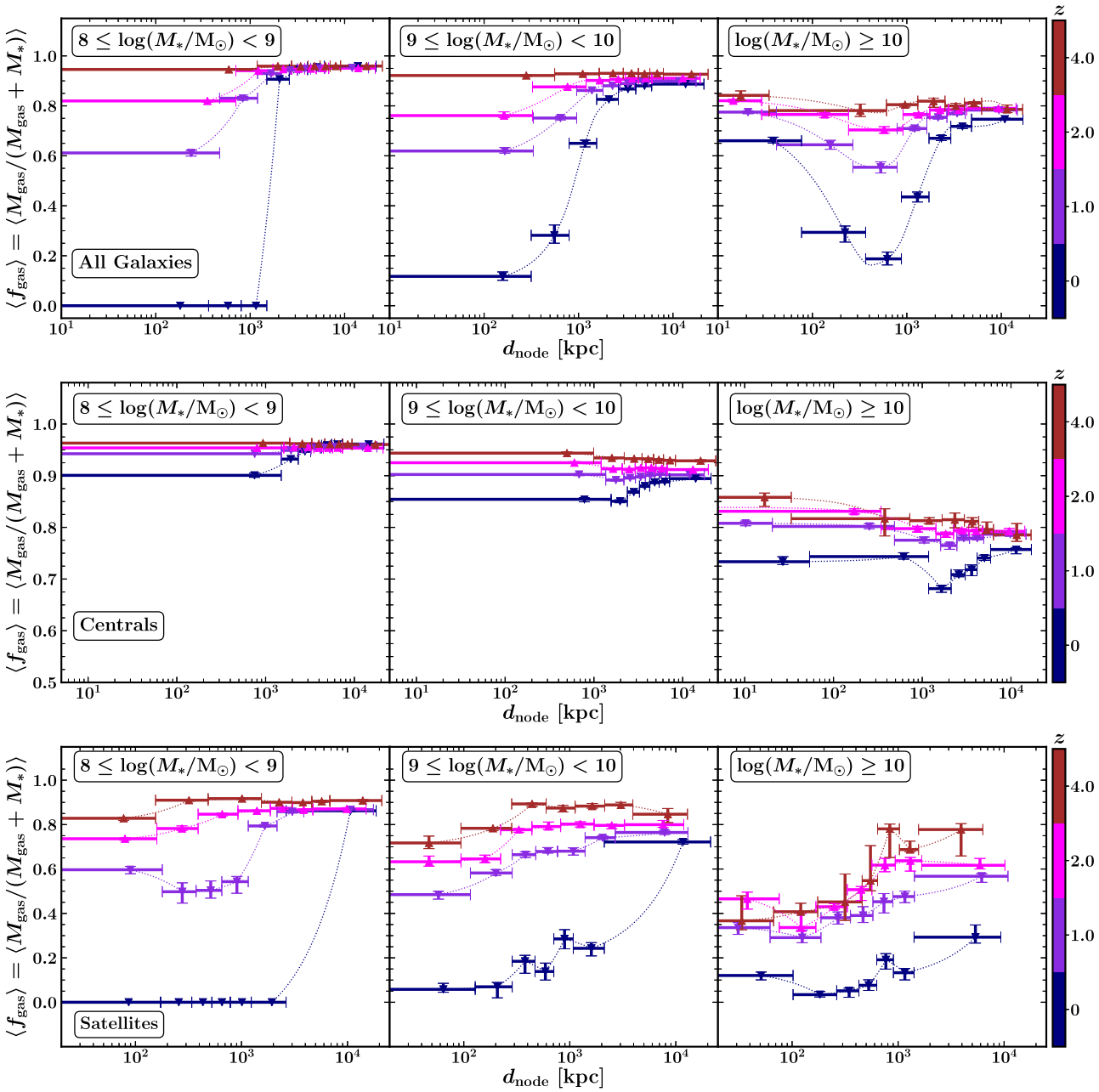

Figure 4. The median gas fraction, $\langle f_{\rm gas}\rangle$, as a function of $d_{\rm node}$ for all galaxies (top row), centrals (middle row), and satellites (bottom row) at redshifts $z = 0$, 1, 2, and 4. The general cosmic web dependence of star formation follows from the available gas supply. Satellites drive the gas fraction trends for lower-mass galaxies while both centrals and satellites drive the high-mass trends.

$\lesssim$500 Myr (e.g., Bahé & McCarthy 2015; Marasco et al. 2016). Here, we find that low-mass satellites close to nodes are already quenched at $z = 0.5$ and have greatly reduced gas fractions at $z = 1$, meaning that the quenched satellites in the local universe have been quenched much earlier. In fact, Donnari et al. (2021) found that in TNG, a large fraction of $z = 0$ $\log(M_*/M_\odot) \lesssim 10$ satellites in groups and clusters were members of other halos where they experienced environmental quenching before falling into their final host—a phenomenon dubbed "preprocessing" (see also, e.g., Fujita 2004; Hou et al. 2014).

AGN feedback from massive central galaxies in groups and clusters may also play an important role in quenching star formation in satellites. The TNG model allows for both "ejective" feedback, whereby BHs expel star-forming gas from a galaxy, and "preventative" feedback, whereby BHs heat up the gas and prevent star formation on longer timescales (Zinger et al. 2020). Both of these modes of AGN feedback have been observed in galaxies near and far (e.g., Fabian 2012; King & Pounds 2015). In particular, Martín-Navarro et al. (2019) showed that stronger BH feedback produces hotter group/cluster media, which make quenching more efficient in satellites. While beyond the scope of this work, it would be valuable to understand how central BH properties such as mass and accretion rate might relate to the cosmic web dependence of star formation.

Satellites at close filament-centric distances and $d_{\rm node} > 1$ Mpc would reside in more intermediate density environments than those at close node-centric distances. In either of these types of environments, fresh gas accretion onto the ISM can be stopped by strangulation/starvation such that star formation

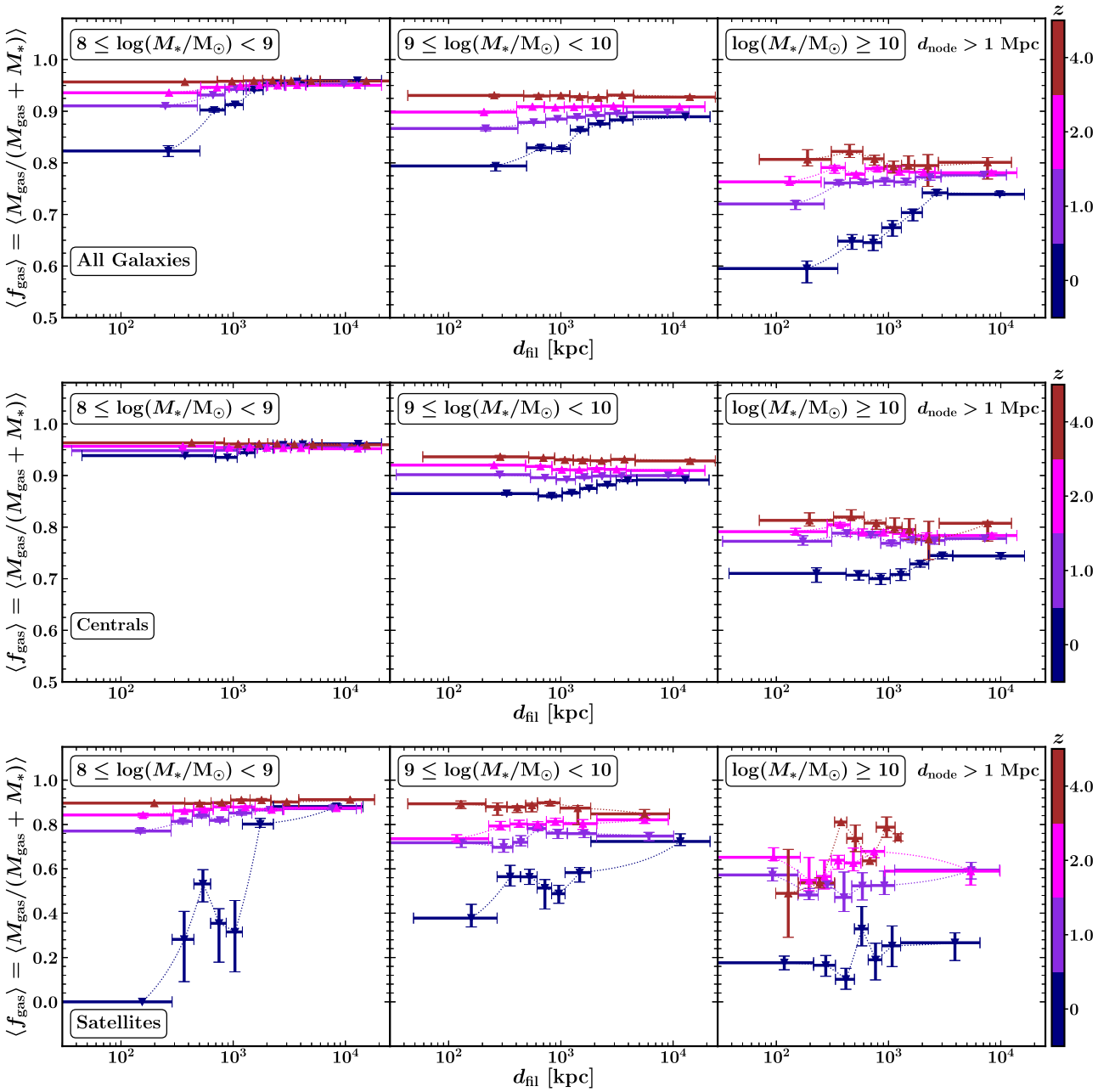

Figure 5. Same as Figure 4, but in bins of $d_{\rm fil}$. Satellites drive the dependence of $\langle f_{\rm gas} \rangle$ on $d_{\rm fil}$ more than centrals.

quenches over longer timescales of about a few Gyr (e.g., Peng et al. 2015; Zinger et al. 2018). In a comprehensive analysis of nearby galaxies, Trussler et al. (2020) found that starvation is likely to be the initial prerequisite for quenching across virtually all masses but the remaining cold ISM gas needs to be heated or ejected to complete the quenching process. Low-mass centrals, on the other hand, exhibit a modest cosmic web dependence on gas fraction and consequently on star formation. For these galaxies, so-called "mass quenching" via internal processes (such as feedback) may dominate over environmental effects (e.g., Peng et al. 2010).

In our investigation, we consider the total content of all gas gravitationally bound to a galaxy, without regard to the physical conditions or location of the gas. For instance, we do not measure the fraction of *cool* gas, which would in principle be a more direct measure of gas supply available for star formation. Regardless, we find that the gas fraction of low-mass satellites declines dramatically from $z = 1$ to $z = 0$ at small $d_{\rm node}$ and to a lesser, but still significant, extent at small $d_{\rm fil}$, indicating a lack of accretion from the IGM to the CGM. Many hydrodynamical simulations indeed show that accretion of cold gas from the IGM becomes increasingly inefficient over time (e.g., Anglés-Alcázar et al. 2017; Hafen et al. 2020). Furthermore, gas in the CGM may be heated substantially or even ejected by SNe (e.g., Pandya et al. 2022) or AGNs (as discussed above) to prevent accretion onto the ISM.

In low-redshift $\log(M_*/M_\odot) \geqslant 10$ galaxies, a minimum in gas fraction and star formation activity occurs at $d_{\rm node} \sim 0.2$ Mpc, following an unexpected rise at smaller $d_{\rm node}$. This upturn in $f_{\rm gas}$ and sSFR close to nodes persists out to $z = 2$, but manifests in an analogous relationship between star formation and proximity to nodes at $z \leqslant 1$. When we limit our sample to even higher-mass

galaxies, this effect is further accentuated, implying that the highest-mass galaxies are primarily responsible. The effect of enhanced star formation very close to nodes is stronger in satellites than in centrals at $z = 0$ while the converse is true at $z = 0.5$–1. The fact that both $\langle \mathrm{sSFR} \rangle$ and $\langle f_{\mathrm{gas}} \rangle$ are lowest at $d_{\mathrm{node}} \sim 0.2$ Mpc implies that massive galaxies falling into groups/clusters from the outskirts are more gas-poor and passive relative to galaxies at the center.

It is conceivable that some/much of the gas removed from low-mass satellites in rich groups and clusters ends up in higher-mass galaxies, enabling the massive galaxies to form stars at higher rates near the centers of these halos. The cores of many groups and clusters have been observed to be abundant in cold gas, which may temporarily trigger star formation near the center (e.g., McDonald et al. 2012; Olivares et al. 2019). However, this gas is also hypothesized to feed central AGN activity and eventually curtail star formation (see Donahue & Voit 2022, and references therein). Heating from the central AGN could explain why the rise in star formation at small d_{node} is not as dramatic as the rise in gas fraction in high-mass galaxies.

The enhancement of star formation in dense environments is not typically observed in statistical studies of the cosmic web–galaxy connection (e.g., Kraljic et al. 2018; Winkel et al. 2021). But there is evidence—both in observations (e.g., Roediger et al. 2014) and in simulations (e.g., Nelson et al. 2018)—of galaxies in groups/clusters enjoying brief episodes of star formation via compression of gas from ram pressure, mergers, or other processes, a phenomenon sometimes called "rejuvenation." However, these events are rare in TNG, with only 10% of $\log(M_*/M_\odot) > 11$ galaxies and 6% of all galaxies at $z = 0$ ever having experienced them (Nelson et al. 2018). An analysis of satellite galaxies by Martín-Navarro et al. (2021) showed that AGN outflows can clear out the CGM of massive halos, which reduces ram pressure and preserves star formation in satellites along the direction of the outflows (the minor axis of the central). These phenomena of *positive* AGN feedback can potentially boost star formation in dense environments such as those close to nodes.

It is also possible that the high-density upturn in star formation is a result of some additional mechanism in the simulations funneling too much gas into galaxies, overcooling the gas, or otherwise reducing the efficiency of quenching at the highest-density environments. Donnari et al. (2021) reported that TNG galaxies in dense environments have diverse histories and quenching pathways that may complicate the interpretation of how and when they quench. Moreover, the AGN-driven gas expulsion in TNG is known to be so efficient that there are very few galaxies with intermediate sSFRs (i.e., Green Valley galaxies; e.g., Schawinski et al. 2014), creating tension with observations (Terrazas et al. 2020).

4.1.2. No Cosmic Web Dependence before Cosmic Noon?

There is now a growing body of evidence suggesting that cosmological accretion shocks from the formation of cosmic web structures, similar to those around massive halos, can affect galaxy formation. Birnboim et al. (2016) showed that in filaments with a specific linear mass density, the accretion shocks are unstable. These structures can efficiently siphon cool gas into $10 \lesssim \log(M_{200,\mathrm{c}}/M_\odot) \lesssim 13$ halos at $z = 3$ and $12 \lesssim \log(M_{200,\mathrm{c}}/M_\odot) \lesssim 15$ halos at $z = 0$ (see their Figure 5). According to the stellar-to-halo-mass relations at these redshifts (e.g., Behroozi et al. 2019), this means that unstable filaments can potentially enhance star formation in galaxies of virtually all masses we study at higher redshifts, while at lower redshifts only the most massive galaxies would see an increase in star formation via this channel. This phenomenon is a possible pathway for early galaxies close to filaments and nodes to have their sSFRs elevated to levels comparable to those far from filaments and nodes.

This explanation necessitates an environmental dependence of *overall star formation activity* at high z instead of specifically *quenching*. The net trend of constant sSFR with distance from the cosmic web could be naively interpreted as quenching processes being environment-independent at high z. As noted in Section 3.3, we find evidence of star formation in satellites close to nodes being more efficient than that in galaxies further away at early times ($z \geqslant 2$). A plausible scenario for this is that gas is more efficiently channeled into the centers of nodes, and eventually the centers of galaxies, via cold streams at high redshift (e.g., Dekel et al. 2009).

Cosmological accretion shocks can also suppress star formation in galaxies. Zinger et al. (2018) showed that accretion shocks at the outskirts of galaxy clusters can quench satellites, which likely impacts galaxies near nodes in our analysis. In TNG, Li et al. (2023) found that shock-induced stripping of the ISM and CGM can quench low-mass satellites inside clusters at $z < 0.11$. Recently, Pasha et al. (2023) found that $5.5 < \log(M_*/M_\odot) < 8.5$ central galaxies at $z = 2$–5 can be quenched by shock-heated cosmic sheets (which eventually collapse into filaments and nodes; e.g., Bond et al. 1996). These shocks directly raise the ambient gas temperature in the vicinity of the sheets and suppress gas accretion and star formation in surrounding galaxies.

The impact of accretion shocks in filaments and nodes on galaxy quenching, as a function of both stellar mass and redshift, may be central to interpreting the results of this paper and therefore deserves detailed investigation. In a follow-up study, we will address this problem by analyzing the gaseous conditions of filaments and nodes—with particular emphasis on accretion shock signatures—in tandem with properties of the galaxies residing within them across cosmic time. This analysis will also allow us to characterize filaments and nodes in more detail and account for the fact that not all filaments or nodes will have the same effect on galaxy formation (e.g., Galárraga-Espinosa et al. 2020 found short and long filaments in TNG to be statistically different populations).

4.1.3. Other Important Physical Considerations

Angular momentum is another important aspect of galaxy formation that may shed additional light on how quenching is affected by the cosmic web. From their analysis of quenching timescales in TNG, Walters et al. (2022) suggested that low angular momentum gas accretion leads to galaxies quenching faster than high angular momentum accretion. In the cosmic web framework, galaxies form in the vorticity-rich regions of filaments, acquire angular momentum, and drift to the nodes (e.g., Dubois et al. 2014; Codis et al. 2015). Simulations have predicted for many years that at $z \gtrsim 1.5$, gas and angular momentum are funneled through cold filamentary streams into the centers of galaxies (e.g., Dekel et al. 2009; Pichon et al. 2011). Over time, as these streams disappear due to heating or other processes, the efficiency of galaxy formation at the centers of filaments and nodes may also decline, potentially

explaining the difference in star formation activity in these regions between low and high redshift. Additionally, galactic properties such as mass and sSFR have been found to be correlated with the acquisition of angular momentum from the cosmic web (e.g., Kraljic et al. 2019; Welker et al. 2020). Thus, a complete understanding of how the cosmic web affects quenching needs to account for angular momentum acquisition in galaxies in tandem with proximity to cosmic web structures.

Many of the relationships between star formation and the cosmic web environment may result from the assembly of DM halos. Subhalo abundance matching predictions from ΛCDM cosmology are found to agree with observed SDSS galaxy distributions, implying that the local density dependence of galaxy properties stems from the corresponding density dependence of halo properties (Dragomir et al. 2018). In the Bolshoi–Planck simulations, Lee et al. (2017) found that for $\log(M_{200,c}/M_{\odot}) \lesssim 12$ halos, halo accretion is higher in low-density environments at $z \lesssim 1$ and in high-density environments at $z \gtrsim 1$. However, some *N*-body simulations have shown that DM halo properties are independent of cosmic web location at fixed overdensities (e.g., Goh et al. 2019). A detailed analysis of the dependence of halo mass accretion on the cosmic web environment in TNG is necessary to disentangle the effect of halo mass growth from baryonic effects in determining the galaxy quenching–cosmic web connection.

4.2. Other Caveats

We consider certain other aspects of our methodology that may affect the robustness of our results as well as the conclusions we draw. The first is how the numerical resolution in the simulation may affect our results. Galárraga-Espinosa et al. (2021) showed that despite the ∼8 times difference in resolution between TNG300-1 and TNG300-2, there are only minor differences in the distribution (including the DisPerSE reconstruction) and properties of filaments. The large scales of the cosmic web are likely to be well resolved with any of the TNG runs, but the smaller scales of galaxy formation are more sensitive to resolution. Thus, it would be interesting to compare our results for TNG100-1 with those for TNG50-1, which has ∼16 times the particle mass resolution of TNG100-1 (e.g., Nelson et al. 2019b, 2020).

The input physics model is another potential source of uncertainty for theoretical galaxy evolution studies. Galárraga-Espinosa et al. (2020) found that different baryonic physics implemented in different simulations result in somewhat different matter distributions around filaments but that gravity is still the dominant driver. Xu et al. (2020) investigated the sSFR of galaxies in filaments, nodes, sheets, and voids in the EAGLE simulation, which uses somewhat different hydrodynamics and feedback prescriptions from the TNG model (see Schaye et al. 2015). They found that at $z < 1$, galaxies with $\log(M_*/M_{\odot}) \lesssim 10.5$ are less star-forming in nodes than in other cosmic web environments, while for more massive galaxies there is virtually no cosmic web dependence, the latter finding being at odds with our results. At $z > 1$, they found no statistical dependence of sSFR on the cosmic web environment, consistent with our findings. In a separate study, Rosas-Guevara et al. (2022) found that the star-forming fraction of $\log(M_*/M_{\odot}) > 9$ galaxies in EAGLE decreases with distance to the nearest void at $z = 0$. It would be interesting to apply our methodology to investigate the evolving cosmic web dependence of star formation in other hydrodynamical cosmological simulations such as SIMBA (Davé et al. 2019) and Horizon-AGN (Dubois et al. 2014). Such comparisons might help illuminate the effect of uncertain baryonic processes such as AGN feedback on the relationship between galaxy formation and the cosmic web.

Another crucial check on our results is the cosmic web reconstruction itself. As mentioned in Section 2.2, we experiment with DisPerSE parameter choices such as persistence and smoothing of the filamentary skeleton. The latter does not have any significant effect on our results and varying the former affects the frequency of identified structures but does not affect any qualitative conclusions. Overall, we consider our results to be robust to parameter choices. There are several other cosmic web reconstruction techniques that have been employed for cosmic web studies, which have advantages and disadvantages over the DisPerSE framework (see Libeskind et al. 2018 for a detailed comparison of many of these methods). We are currently applying a new state-of-the-art cosmic web reconstruction algorithm called the Monte Carlo Physarum Machine (MCPM), inspired by the *Physarum polycephalum* (slime mold) organism (Elek et al. 2021, 2022), to compare to the local density estimation and global cosmic web characterization from DisPerSE. This method produces continuous cosmic matter densities (as opposed to discrete DTFE densities at the locations of galaxies) and has been applied successfully to both theoretical and observational data sets (e.g., Burchett et al. 2020; Simha et al. 2020; Wilde et al. 2023).

We also assess the importance of local galaxy overdensity in shaping the star formation–cosmic web connection. We repeat our analyses in Section 3 by only considering galaxies with local DTFE galaxy overdensity (as computed by DisPerSE) within $\pm 1\sigma$ of the mean. We find that the resulting relationships with respect to $d_{\rm node}$ and $d_{\rm fil}$ look strikingly similar to those we report without filtering out galaxies by overdensity, implying that the effect of cosmic web environment on star formation persists beyond just the highest-density regions of the universe. However, we stress that local overdensity and the global cosmic web environment are necessarily related to each other and it is therefore not trivial to disentangle the effects of one from those of the other. We defer a detailed characterization of the dependence of $d_{\rm fil}$ and $d_{\rm node}$ on overdensity across different redshifts in TNG100 to a future work (see Malavasi et al. 2022 for an in-depth mapping of overdensity to cosmic web proximity in TNG300).

Finally, in our interpretations, we neglect the effect of pseudo-evolution of filaments and nodes, i.e., the evolution of the reference density (in our case, the DTFE mean density) instead of a true *physical* density. Such pseudo-evolution is known to strongly drive the mass evolution in DM halos, especially at lower redshifts (Diemer et al. 2013), and we defer a detailed investigation of this effect to future work.

4.3. Testing Predictions with Observations

The predictions presented herein from the TNG100 simulation establish clear objectives for observational studies. First, we identify a point in cosmic time when galaxies' star formation activity begins to depend on their location relative to the large-scale cosmic web environment. Confronting this prediction with observations will necessitate wide-field galaxy surveys capable of characterizing the large-scale structure over

a large range of redshifts, out to at least $z = 2$. Second, a common theme we observe in both sSFR and gas fraction is an increase at small node-centric distances for high-mass galaxies. This will require the extensive survey data necessary for both finding these galaxies and, perhaps even more challenging, measuring their gas content. Spectroscopic galaxy surveys both underway and planned for the next several years should make serious headway toward at least the first element of this challenging observational experiment.

The current gold standard for wide-field spectroscopic surveys is SDSS, which can provide the lowest-redshift anchor point for such a comparison. The quoted SDSS spectroscopic completeness limit of $m_r = 17.7$ would correspond to a redshift limit of $z \sim 0.01$ for the lowest-mass galaxies studied here ($10^8\,M_\odot$). Even at $z \sim 0.1$, SDSS is only complete to $\sim 10^{10}\,M_\odot$, covering the most massive bin we study. Thus, SDSS, in principle, is capable of yielding measurements comparable with the dark blue data points in Figures 2 and 3. Although an independent analysis of observational data sets with our methodology is beyond the scope of this paper, we can refer the reader to the work of Kuutma et al. (2017), Crone Odekon et al. (2018), and Winkel et al. (2021), who explored similar relationships with SDSS. Also of note is the study of Kraljic et al. (2018), who employed the Galaxy and Mass Assembly (GAMA) survey, which goes 2 mag deeper than SDSS, albeit over a much smaller volume. Still, this does not push completeness to the $z > 1$ transition point in cosmic web dependence we report here.

Constraining the higher redshifts will be more difficult, although the various Dark Energy Spectroscopic Instrument (DESI) surveys should enable cosmic web reconstructions at intermediate redshifts. Initial data and results from the survey validation phase are beginning to be released now, showing promising prospects for mapping the large-scale structure to $z \sim 0.5$ for the Bright Galaxy Survey, to $z \sim 1.1$ for the luminous red galaxies (LRGs), to $z \sim 1.6$ for the emission-line galaxies (ELGs), and possibly beyond (Lan et al. 2023, and references therein). However, each of these samples is likely to contain highly biased tracers of the underlying structure, e.g., LRGs are by definition passive galaxies and will preferentially reside in the most massive halos, likely tracing nodes. Conversely, the ELGs, being vigorously star-forming, might bias against these very environments. Nevertheless, neither of these samples will suitably represent the full diversity in star formation exhibited by the general population. Deep follow-up surveys with more agnostic selection criteria will be necessary for a fair comparison with our results.

The Subaru Prime Focus Spectrograph (PFS) also offers great promise for mapping out the galaxy–cosmic web connection at higher redshifts (Takada et al. 2014). In particular, the PFS Galaxy Evolution program will observe up to half a million galaxies at redshifts $0.7 \lesssim z \lesssim 7$ (Greene et al. 2022). The largest survey of this program is expected to yield $>10^5$ continuum-selected galaxies down to a stellar mass limit of $\log(M_*/M_\odot) \approx 10.5$ over a comoving survey volume of ~ 0.1 Gpc^3 ($\sim$100 times the TNG100 volume) at $0.7 \lesssim z \lesssim 2$. Stellar masses, SFRs, and gas properties will be measured for the vast majority of these galaxies. This sample will be complemented by a smaller number of Lyman-break galaxies and Lyα emitters out to $z \sim 7$, which would be more biased tracers of the cosmic web as discussed above.

Spectroscopic surveys with JWST and eventually with the Nancy Grace Roman Space Telescope will yield galaxy data sets ripe for placing into context with the cosmic web mapped by DESI and Subaru PFS. Roman, which will map 1700 deg^2 of the sky at infrared wavelengths via the High Latitude Spectroscopic Survey (Wang et al. 2022), should reveal the cosmic web over scales of $\sim$1 Gpc as well as the galaxies out to $z \sim 2$. In the shorter term, JWST, through programs such as JADES (Cameron et al. 2023), will yield galaxy spectra to $z > 5$ albeit over much smaller fields of view (the JWST Microshutter Assembly will map scales $\sim$1 Mpc in a single pointing). An amalgamation of several such deep fields will be necessary to mitigate cosmic variance.

5. Conclusion

In this study, we investigated the IllustrisTNG simulations to understand how the star formation activity of galaxies depends on their cosmic web environment. We used all $\log(M_*/M_\odot) \geqslant 8$ galaxies to reconstruct the cosmic web in the TNG100 snapshots using the DisPerSE framework. We measured the median sSFR and median $f_{\rm gas}$ of the galaxies as functions of distance to the nearest cosmic web node ($d_{\rm node}$) and filament spine ($d_{\rm fil}$). Our main results are as follows:

1. The $\langle$sSFR$\rangle$ of galaxies at any mass only depends on $d_{\rm node}$ or $d_{\rm fil}$ at redshifts $z \lesssim 2$; the median star formation is independent of the cosmic web environment at $z \geqslant 2$. This holds true also for central and satellite galaxies separately.
2. In $\log(M_*/M_\odot) < 10$ galaxies, $\langle$sSFR$\rangle$ increases monotonically with $d_{\rm node}$ at $z \leqslant 1$, with $8 \leqslant \log(M_*/M_\odot) < 9$ galaxies being completely quenched at $d_{\rm node} < 1$ Mpc at $z \leqslant 0.5$. $\langle$sSFR$\rangle$ has a shallower increase with $d_{\rm fil}$ at these redshifts. These trends are almost entirely driven by satellites.
3. In $\log(M_*/M_\odot) \geqslant 10$ galaxies, the $\langle$sSFR$\rangle$–$d_{\rm node}$ relationship inverts at $d_{\rm node} \lesssim 0.2$ Mpc up to $z = 1$, while the $\langle$sSFR$\rangle$–$d_{\rm fil}$ relation does not. The $\langle$sSFR$\rangle$–$d_{\rm node}$ inversion is driven by both satellites and centrals, but the $\langle$sSFR$\rangle$–$d_{\rm fil}$ relationship is due to satellites.
4. Most of these star formation–cosmic web relationships can be explained by the cosmic web dependence of the gas fraction in galaxies, although there is evidence of $\langle f_{\rm gas}\rangle$ depending more strongly on the cosmic web environment than $\langle$sSFR$\rangle$ in some cases.

Our results point to a picture where the influence of the cosmic web environment on quenching galaxies is first established at $z \sim 2$. In the last $\sim$10 Gyr, low-mass dwarf satellites are quenched by their star-forming gas supply being depleted either on short timescales (e.g., via ram pressure stripping or outflows) or on longer timescales (e.g., via starvation), while star formation in low-mass centrals is far less affected by the cosmic web environment. At this epoch, high-mass galaxies at the centers of nodes are more gas-rich and star-forming than their counterparts at the outskirts, which could be due to temporary rejuvenation events, positive AGN feedback, and/or the TNG model itself. In the earlier universe (>10 Gyr ago), cosmic web structures likely aided star formation more than they suppressed it, possibly via unstable filaments feeding cold gas to galaxies or cold streams efficiently funneling initially high angular momentum gas to the central regions of filaments and nodes.

In a follow-up study, we will investigate how the gaseous physical conditions of filaments and nodes affect galaxy formation in TNG100, particularly how accretion shocks around filaments and nodes affect star formation. Furthermore, we will compare the cosmic web reconstruction from DisPerSE with that from the novel MCPM algorithm (Elek et al. 2021, 2022) to obtain more fine-grained insights into the global and local environmental dependence of star formation across cosmic time. The results of this work provide important predictions to test against ongoing large spectroscopic surveys such as SDSS and DESI, as well as against ongoing and planned surveys with Subaru PFS, JWST, and Roman.

Acknowledgments

We are very grateful to N. Luber and Z. Edwards for their help with setting up DisPerSE. We thank the anonymous referee for helpful comments that improved the quality of this manuscript. We thank the attendees of the 2022 Santa Cruz Galaxy Workshop and the 2023 KITP Cosmic Web Conference, including F. van den Bosch, J. Woo, H. Aung, J. Powell, C. Pichon, U. Kuchner, C. Welker, S. Simha, K.-G. Lee, and R. Momose, for stimulating and interesting conversations on this work. F.H., J.N.B., and A.A. are supported by the National Science Foundation LEAPS-MPS award #2137452. O.E. is supported by an incubator fellowship of the Open Source Program Office at UC Santa Cruz funded by the Alfred P. Sloan Foundation (G-2021-16957). D.N. is supported by NSF (AST-2206055) and NASA (80NSSC22K0821 and TM3-24007X) grants.

ORCID iDs

Farhanul Hasan https://orcid.org/0000-0002-0072-0281
Joseph N. Burchett https://orcid.org/0000-0002-1979-2197
Alyssa Abeyta https://orcid.org/0009-0007-2588-9407
Nir Mandelker https://orcid.org/0000-0001-8057-5880
Joel R. Primack https://orcid.org/0000-0001-5091-5098
S. M. Faber https://orcid.org/0000-0003-4996-214X
David C. Koo https://orcid.org/0000-0003-3385-6799
Oskar Elek https://orcid.org/0000-0003-0549-3302
Daisuke Nagai https://orcid.org/0000-0002-6766-5942

References

Anglés-Alcázar, D., Faucher-Giguère, C.-A., Kereš, D., et al. 2017, MNRAS, 470, 698
Aragon Calvo, M. A., Neyrinck, M. C., & Silk, J. 2019, OJAp, 2, 7
Bahé, Y. M., & McCarthy, I. G. 2015, MNRAS, 447, 969
Balogh, M. L., & Morris, S. L. 2000, MNRAS, 318, 703
Behroozi, P., Wechsler, R. H., Hearin, A. P., & Conroy, C. 2019, MNRAS, 488, 3143
Birnboim, Y., Padnos, D., & Zinger, E. 2016, ApJL, 832, L4
Bluck, A. F. L., Maiolino, R., Sánchez, S. F., et al. 2020, MNRAS, 492, 96
Bond, J. R., Kofman, L., & Pogosyan, D. 1996, Natur, 380, 603
Boselli, A., Fossati, M., & Sun, M. 2022, A&ARv, 30, 3
Boselli, A., & Gavazzi, G. 2006, PASP, 118, 517
Brinchmann, J., Charlot, S., White, S. D. M., et al. 2004, MNRAS, 351, 1151
Burchett, J. N., Elek, O., Tejos, N., et al. 2020, ApJL, 891, L35
Cameron, A. J., Saxena, A., Bunker, A. J., et al. 2023, arXiv:2302.04298
Cattaneo, A., Dekel, A., Devriendt, J., Guiderdoni, B., & Blaizot, J. 2006, MNRAS, 370, 1651
Chang, W., Fang, G., Gu, Y., et al. 2022, ApJ, 936, 47
Codis, S., Pichon, C., & Pogosyan, D. 2015, MNRAS, 452, 3369
Crone Odekon, M., Hallenbeck, G., Haynes, M. P., et al. 2018, ApJ, 852, 142
Croton, D. J., Springel, V., White, S. D. M., et al. 2006, MNRAS, 365, 11
Darvish, B., Mobasher, B., Sobral, D., et al. 2016, ApJ, 825, 113
Darvish, B., Sobral, D., Mobasher, B., et al. 2014, ApJ, 796, 51
Davé, R., Anglés-Alcázar, D., Narayanan, D., et al. 2019, MNRAS, 486, 2827
Dekel, A., & Birnboim, Y. 2006, MNRAS, 368, 2
Dekel, A., Birnboim, Y., Engel, G., et al. 2009, Natur, 457, 451
Diemer, B., More, S., & Kravtsov, A. V. 2013, ApJ, 766, 25
Dolag, K., Borgani, S., Murante, G., & Springel, V. 2009, MNRAS, 399, 497
Donahue, M., & Voit, G. M. 2022, PhR, 973, 1
Donnari, M., Pillepich, A., Joshi, G. D., et al. 2021, MNRAS, 500, 4004
Dragomir, R., Rodríguez-Puebla, A., Primack, J. R., & Lee, C. T. 2018, MNRAS, 476, 741
Dubois, Y., Pichon, C., Welker, C., et al. 2014, MNRAS, 444, 1453
Eardley, E., Peacock, J. A., McNaught-Roberts, T., et al. 2015, MNRAS, 448, 3665
Elbaz, D., Daddi, E., Le Borgne, D., et al. 2007, A&A, 468, 33
Elek, O., Burchett, J. N., Prochaska, J. X., & Forbes, A. G. 2021, IEEE Trans. Vis. and Comput. Graph., 27, 806
Elek, O., Burchett, J. N., Prochaska, J. X., & Forbes, A. G. 2022, Artif. Life, 28, 22
Fabian, A. C. 2012, ARA&A, 50, 455
Fujita, Y. 2004, PASJ, 56, 29
Gabor, J. M., & Davé, R. 2012, MNRAS, 427, 1816
Galárraga-Espinosa, D., Aghanim, N., Langer, M., Gouin, C., & Malavasi, N. 2020, A&A, 641, A173
Galárraga-Espinosa, D., Aghanim, N., Langer, M., & Tanimura, H. 2021, A&A, 649, A117
Geha, M., Blanton, M. R., Yan, R., & Tinker, J. L. 2012, ApJ, 757, 85
Goh, T., Primack, J., Lee, C. T., et al. 2019, MNRAS, 483, 2101
Greene, J., Bezanson, R., Ouchi, M., Silverman, J. & the PFS Galaxy Evolution Working Group 2022, arXiv:2206.14908
Hafen, Z., Faucher-Giguère, C.-A., Anglés-Alcázar, D., et al. 2020, MNRAS, 494, 3581
Hou, A., Parker, L. C., & Harris, W. E. 2014, MNRAS, 442, 406
Kereš, D., Katz, N., Fardal, M., Davé, R., & Weinberg, D. H. 2009, MNRAS, 395, 160
Kereš, D., Katz, N., Weinberg, D. H., & Davé, R. 2005, MNRAS, 363, 2
King, A., & Pounds, K. 2015, ARA&A, 53, 115
Kotecha, S., Welker, C., Zhou, Z., et al. 2022, MNRAS, 512, 926
Kraljic, K., Arnouts, S., Pichon, C., et al. 2018, MNRAS, 474, 547
Kraljic, K., Pichon, C., Dubois, Y., et al. 2019, MNRAS, 483, 3227
Kuutma, T., Tamm, A., & Tempel, E. 2017, A&A, 600, L6
Laigle, C., Pichon, C., Arnouts, S., et al. 2018, MNRAS, 474, 5437
Lan, T.-W., Tojeiro, R., Armengaud, E., et al. 2023, ApJ, 943, 68
Larson, R. B., Tinsley, B. M., & Caldwell, C. N. 1980, ApJ, 237, 692
Lee, C. T., Primack, J. R., Behroozi, P., et al. 2017, MNRAS, 466, 3834
Li, H., Wang, H., Mo, H. J., et al. 2023, ApJ, 942, 44
Libeskind, N. I., van de Weygaert, R., Cautun, M., et al. 2018, MNRAS, 473, 1195
Madau, P., & Dickinson, M. 2014, ARA&A, 52, 415
Malavasi, N., Langer, M., Aghanim, N., Galárraga-Espinosa, D., & Gouin, C. 2022, A&A, 658, A113
Marasco, A., Crain, R. A., Schaye, J., et al. 2016, MNRAS, 461, 2630
Marinacci, F., Vogelsberger, M., Pakmor, R., et al. 2018, MNRAS, 480, 5113
Martín-Navarro, I., Burchett, J. N., & Mezcua, M. 2019, ApJL, 884, L45
Martín-Navarro, I., Pillepich, A., Nelson, D., et al. 2021, Natur, 594, 187
McDonald, M., Bayliss, M., Benson, B. A., et al. 2012, Natur, 488, 349
Momose, R., Lee, K.-G., Horowitz, B., Ata, M., & Kartaltepe, J. S. 2022, arXiv:2212.05984
Moutard, T., Sawicki, M., Arnouts, S., et al. 2018, MNRAS, 479, 2147
Naiman, J. P., Pillepich, A., Springel, V., et al. 2018, MNRAS, 477, 1206
Nelson, D., Pillepich, A., Springel, V., et al. 2018, MNRAS, 475, 624
Nelson, D., Pillepich, A., Springel, V., et al. 2019b, MNRAS, 490, 3234
Nelson, D., Sharma, P., Pillepich, A., et al. 2020, MNRAS, 498, 2391
Nelson, D., Springel, V., Pillepich, A., et al. 2019a, ComAC, 6, 2
Olivares, V., Salome, P., Combes, F., et al. 2019, A&A, 631, A22
Pandya, V., Fielding, D. B., Bryan, G. L., et al. 2022, arXiv:2211.09755
Pasha, I., Mandelker, N., van den Bosch, F. C., Springel, V., & van de Voort, F. 2023, MNRAS, 520, 2692
Peng, Y., Maiolino, R., & Cochrane, R. 2015, Natur, 521, 192
Peng, Y.-j., Lilly, S. J., Kovač, K., et al. 2010, ApJ, 721, 193
Peng, Y.-j., Lilly, S. J., Renzini, A., & Carollo, M. 2012, ApJ, 757, 4
Peng, Y.-j., & Renzini, A. 2020, MNRAS Lett., 491, L51
Pichon, C., Pogosyan, D., Kimm, T., et al. 2011, MNRAS, 418, 2493
Pillepich, A., Springel, V., Nelson, D., et al. 2018, MNRAS, 473, 4077
Planck Collaboration, Ade, P. A. R., & Aghanim, N. 2016, A&A, 594, A13
Renzini, A. 2020, MNRAS Lett., 495, L42
Roediger, E., Bruggen, M., Owers, M. S., Ebeling, H., & Sun, M. 2014, MNRAS Lett., 443, L114

Rosas-Guevara, Y., Tissera, P., Lagos, C. d. P., Paillas, E., & Padilla, N. 2022, MNRAS, 517, 712
Schaap, W. E., & van de Weygaert, R. 2000, A&A, 363, L29
Schawinski, K., Urry, C. M., Simmons, B. D., et al. 2014, MNRAS, 440, 889
Schaye, J., Crain, R. A., Bower, R. G., et al. 2015, MNRAS, 446, 521
Simha, S., Burchett, J. N., Prochaska, J. X., et al. 2020, ApJ, 901, 134
Song, H., Laigle, C., Hwang, H. S., et al. 2021, MNRAS, 501, 4635
Sousbie, T. 2011, MNRAS, 414, 350
Sousbie, T., Pichon, C., & Kawahara, H. 2011, MNRAS, 414, 384
Springel, V. 2010, MNRAS, 401, 791
Springel, V., Pakmor, R., Pillepich, A., et al. 2018, MNRAS, 475, 676
Springel, V., White, S. D. M., Jenkins, A., et al. 2005, Natur, 435, 629
Springel, V., White, S. D. M., Tormen, G., & Kauffmann, G. 2001, MNRAS, 328, 726
Stern, J., Faucher-Giguère, C.-A., Fielding, D., et al. 2021, ApJ, 911, 88
Stern, J., Fielding, D., Faucher-Giguère, C.-A., & Quataert, E. 2020, MNRAS, 492, 6042
Strauss, M. A., Weinberg, D. H., Lupton, R. H., et al. 2002, AJ, 124, 1810
Takada, M., Ellis, R. S., Chiba, M., et al. 2014, PASJ, 66, R1
Terrazas, B. A., Bell, E. F., Pillepich, A., et al. 2020, MNRAS, 493, 1888
Trussler, J., Maiolino, R., Maraston, C., et al. 2020, MNRAS, 491, 5406
Vulcani, B., Poggianti, B. M., Moretti, A., et al. 2019, MNRAS, 487, 2278
Walters, D., Woo, J., & Ellison, S. L. 2022, MNRAS, 511, 6126
Wang, Y., Zhai, Z., Alavi, A., et al. 2022, ApJ, 928, 1
Welker, C., Bland-Hawthorn, J., van de Sande, J., et al. 2020, MNRAS, 491, 2864
Wilde, M. C., Elek, O., Burchett, J. N., et al. 2023, arXiv:2301.02719
Williams, R. J., Quadri, R. F., Franx, M., van Dokkum, P., & Labbé, I. 2009, ApJ, 691, 1879
Winkel, N., Pasquali, A., Kraljic, K., et al. 2021, MNRAS, 505, 4920
Xu, W., Guo, Q., Zheng, H., et al. 2020, MNRAS, 498, 1839
Zheng, H., Liao, S., Hu, J., et al. 2022, MNRAS, 514, 2488
Zinger, E., Dekel, A., Kravtsov, A. V., & Nagai, D. 2018, MNRAS, 475, 3654
Zinger, E., Pillepich, A., Nelson, D., et al. 2020, MNRAS, 499, 768